Radial magnetic compression in the expelled jet of a plasma deflagration accelerator

Cite as: Appl. Phys. Lett. **108**, 094104 (2016); https://doi.org/10.1063/1.4943370
Submitted: 08 December 2015 . Accepted: 24 February 2016 . Published Online: 03 March 2016

Keith T. K. Loebner, Thomas C. Underwood, Theodore Mouratidis, and Mark. A. Cappelli

Radial magnetic compression in the expelled jet of a plasma deflagration accelerator

Keith T. K. Loebner,[a] Thomas C. Underwood, Theodore Mouratidis, and Mark. A. Cappelli
High Temperature Gasdynamics Laboratory, Stanford University, Stanford, California 94305, USA

(Received 8 December 2015; accepted 24 February 2016; published online 3 March 2016)

A spectroscopic study of a pulsed plasma deflagration accelerator is carried out that confirms the existence of a strong compression in the emerging jet at the exit plane of the device. An imaging spectrometer is used to collect broadened Hα emission from a transaxial slice of the emerging jet at high spatial resolution, and the radial plasma density profile is computed from Voigt fits of the Abel inverted emissivity profiles. The plasma temperature, determined via Doppler broadening of impurity line emission, is compared against the temperature predictions of a radial magnetohydrodynamic equilibrium model applied to the measured density profiles. Empirical scaling laws developed for the plasma density, combined with the measured and predicted temperatures, indicate that a radially equilibrated Z-pinch is formed within the expelled plasma jet at the exit plane during the deflagration process. © *2016 AIP Publishing LLC*. [http://dx.doi.org/10.1063/1.4943370]

The operation of pulsed plasma accelerators in the 'gas-puff' mode and the subsequent generation of a plasma deflagration have been studied for several decades.[1–11] The plasma deflagration process is characterized by broad, diffuse current conduction zones within the accelerator, and the expulsion of high velocity collimated plasma jets. These jets are important in a number of physics subfields, such as the replication of astrophysical jets in the laboratory,[12,13] plasma-jet driven magneto-intertial fusion,[14–16] shear-stabilized Z-pinch fusion schemes,[17–19] and advanced space propulsion concepts.[20,21] A thorough understanding of the plasma dynamics and scaling of parameters within the jet is thus of particular interest. In addition, physical mechanisms that may be at work in shaping and affecting the emergent jets deserve close examination. Hence, contrary to diagnostic work in Refs. 2 and 3, and others, we direct our study to the discharge region where the jet emerges from the accelerator.

In this Letter, we present measurements of the conditions at the exit plane of the Stanford Plasma Gun (SPG) experiment, shown in Fig. 1, and demonstrate that they are consistent with the hallmark radial magnetic compression of a Z-pinch. Prior work[22] on the SPG facility has convincingly shown that the accelerated plasma jet is produced by a plasma deflagration,[3] and that the inter-electrode acceleration process is free from the narrow current sheets that are characteristic of typical Z-pinch configurations.[10,23] However, our results show that in spite of the apparent absence of collapsing current sheets, a radially compressed plasma column is generated within the jet at the exit plane of the SPG during the deflagration process.

The plasma source employed for this study is the Stanford Plasma Gun Experiment, shown schematically in Fig. 2(a). This device is a 26 cm long, 5 cm diameter, coaxial pulsed Lorentz force plasma accelerator, a configuration that has been used extensively in earlier work.[3,4,6,8–10] During operation, breakdown is initiated by the injection of a hydrogen gas puff into the breech end of the accelerator (indicated in Fig. 2(a)) using a custom-built gas puff valve.[24] The electrodes of the accelerator are held at high voltage in vacuum, and initial breakdown occurs when gas injection causes the pressure to rise and intersect the Paschen curve. The self-induced magnetic field accelerates the plasma in the axial direction, generating a highly collimated plasma jet.[10,11,22] The current is driven by a 56 μF capacitor bank and takes the form of an underdamped RLC oscillation. Operating voltages between 3–8 kV were used for this study, corresponding to peak currents of ~3–7.5 kA.

The plasma density in the exit plane region of the SPG was determined by measuring the Stark broadening of the Hα emission collected via an imaging spectrometer. As shown in Fig. 2(a), a single lens (10 cm diameter, *f*/2) images the plasma onto the entrance slit, matching the *f*-number of the 0.75 m SPEX 750 M spectrometer using an aperture stop. A 1200 groove/mm grating, blazed at 5°10′, disperses the light; the entrance slit is set to maximum height to avoid cutting off any vertical spatial information. The dispersed light

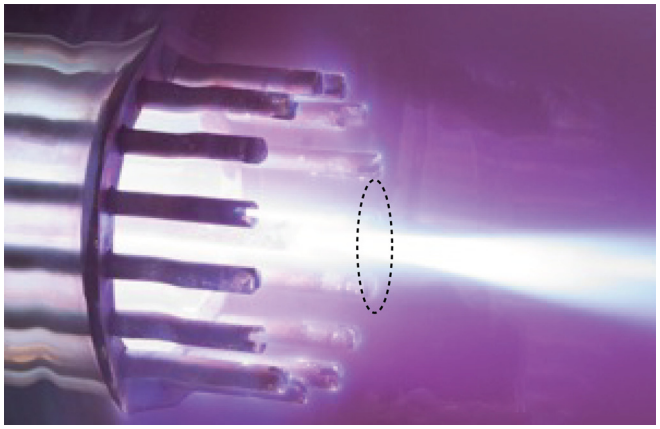

FIG. 1. Time-integrated image (5 s exposure) of the exit plane of the Stanford Plasma Gun during firing. The dotted oval indicates the approximate region from which light is collected by the imaging spectrometer.

[a]Author to correspondence should be addressed. Electronic mail: kloebner@stanford.edu

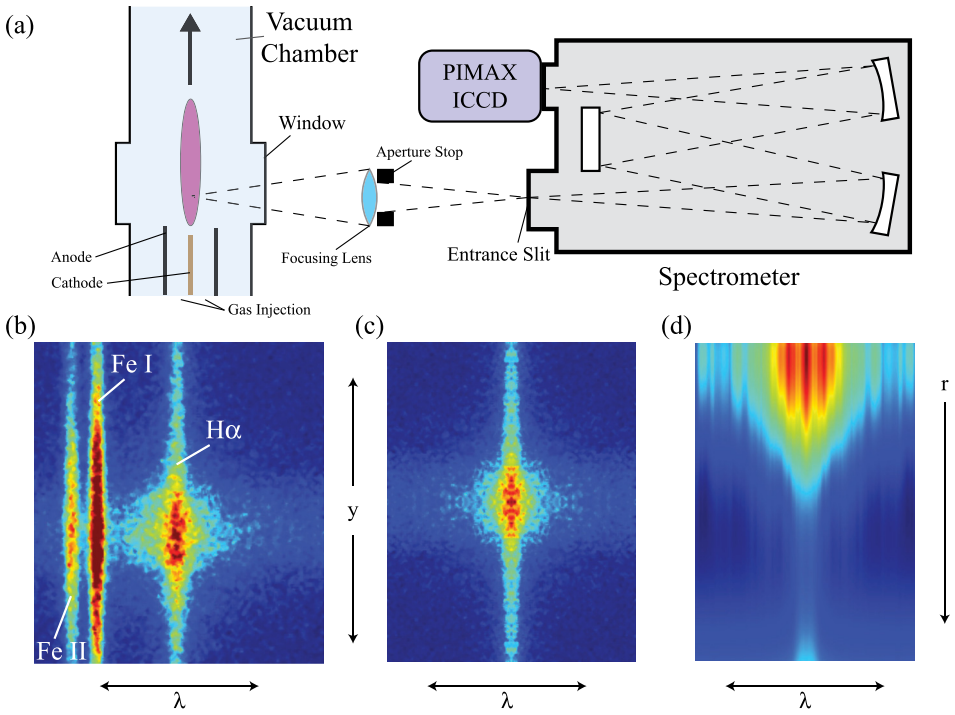

FIG. 2. (a) Schematic of the experimental setup. (b) Example image of chord-integrated intensity as a function of wavelength and vertical height [$I(\lambda, y)$], collected by the PI-MAX camera, including the impurity lines (Fe I and Fe II) and Hα line. (c) Example symmetrized image [based on the upper righthand quadrant in (b)] of chord-integrated intensity as a function of wavelength and vertical height. (d) Abel-inverted emissivity profile vs. radius and wavelength [$\varepsilon(r, \lambda)$], based on the example chord-integrated intensity map in (c).

is then imaged onto a Princeton Instruments PI-MAX intensified CCD camera, which is gateable down to ~2 ns. We determined the wavelength calibration factor (0.125 Å/pixel) and height calibration factor (0.16 mm/pixel) by placing a mercury spectral lamp in the target region (i.e., the region circled in Fig. 1), and focusing on two closely spaced Hg lines (see supplementary material). Two portions of the mercury lamp discharge tube, separated by a known distance, were used to calibrate vertical spatial resolution. The instrument broadening was determined using a hydrogen lamp and used to establish a baseline for deconvolution from broadening due to the plasma. The camera was triggered simultaneously with breakdown of the gas and gated to a 10 μs exposure so as to capture emission exclusively from the deflagration portion of the discharge.[22]

In order to determine the radial profiles of the Hα line emission from the chordwise integrated emission intensity, we utilize the inverse Abel transform, given in analytical form by

$$\varepsilon(r) = -\frac{1}{\pi}\int_r^R \frac{dI(y)}{dy}\frac{dy}{\sqrt{y^2 - r^2}}, \tag{1}$$

where $I(y)$ is the experimentally measured, chord-integrated intensity, R is the radius at which the measured intensity reaches the background level, and $\varepsilon(r)$ is the calculated radial emissivity. To compute Eq. (1), we use the Nestor-Olsen method, summarized by

$$\varepsilon_k(r) = -\frac{2}{\Delta y \pi}\sum_{n-k}^{N-1} I(y_n) B_{k,n}, \tag{2}$$

where the integers k and n are the position indices of the radial and vertical intensities, and Δy is the distance between adjacent experimental data points. For details of the calculation of the weights $B_{k,n}$, see Ref. 25. The Abel transform is highly sensitive to the symmetry of the measured integral data. Accordingly, we symmetrize the measured intensity about the centroid of the Stark broadened Hα emission line, as shown in Fig. 2(c). The upper and lower lefthand quadrants were not considered, due to the frequent smearing of the Hα line into the nearby Fe lines and the resulting difficulty in deconvolving the spectra. Each vertical slice of the symmetrized data was fit with a Gaussian curve and inverted. After the emissivity profile $\varepsilon(\lambda, r)$ was reconstituted from the inverted slices, a Voigt profile was fit to each radial slice. The Lorentzian component of the Voigt fit is due to the Stark broadening, from which the plasma density was calculated using an empirical correlation for the Stark broadening of hydrogen.[26] The Gaussian component of the Voigt fit converged inconsistently and was negligible at most r-values, and so it was not used to determine the temperature. Trials where a significant fraction of radial slices had a greater fitting error than 5% were excluded.

The plasma temperature was estimated by measuring the Doppler broadening of the impurity lines that were visible on the captured images of the Hα line, as shown in Fig. 2(b). The Fe I line at 656.92 nm was used in lieu of the Fe II line at 657.14 nm, as a more consistent signal was obtained from the former.[27] Assuming the impurity species to be in a Maxwell-Boltzmann distribution, the temperature is given from the Doppler width by

$$T = \left(\frac{\Delta\lambda}{2\lambda_0}\right)^2 \frac{mc^2}{2k_B \ln 2}, \tag{3}$$

where $\Delta\lambda$ is the full-width at half maximum of the spectral line intensity distribution, λ_0 is the center wavelength, m is the ion mass, c is the speed of light in vacuum, and k_B is the Boltzmann constant. Assuming that the impurity species are in local thermal equilibrium (LTE) with the ions of the bulk plasma (as they would be in a highly collisional pinch or

focus), then this provides an estimate of the bulk plasma temperature.

In order to show a consistent relationship between the measured plasma temperature and plasma density distribution, we employ an equilibrium Z-pinch model that captures the radial compression of the plasma at the exit plane. The constant drift velocity (CDV) equilibrium Z-pinch model has been shown to correspond well to a high energy shear-stabilized Z-pinch.[28] By applying the model to our device, we seek to show support for the existence of a radially-equilibrated Z-pinch in the core of the expelled jet. From the CDV assumption, which constrains the current density to be proportional to the number density (i.e., $j = Cn_e$), the azimuthal B-field is determined from Ampere's law

$$B_\theta(r) = \frac{\mu_0}{r}\int_0^r j(r')r'dr', \tag{4}$$

where the proportionality constant C is determined from the number density profile and the measured discharge current (assumed to be the axial current in the focus), i.e.

$$C = \frac{I}{\int_0^{2\pi}\int_0^a n_e(r)rdrd\theta}. \tag{5}$$

In the absence of an applied axial field, equilibrium in a radially compressed plasma column is given by

$$\frac{dp}{dr} = -\frac{B_\theta(r)}{\mu_0 r}\frac{d[rB_\theta(r)]}{dr} \tag{6}$$

which can be solved to yield $p(r)$, which in turn can be combined with the ideal gas law and the measured $n_e(r)$ to provide the temperature profile, i.e.

$$T(r) = \frac{p(r)}{(1+1/Z)n_e k}. \tag{7}$$

Here, Z is the ionization state of the bulk plasma ions (assumed to be $Z = 1$ for hydrogen).

A series of example radial density curves calculated from the Abel-inverted emissivity profiles is shown in Fig. 3(a). The curves calculated from the lower righthand (LR) quadrant of the symmetrized intensity distribution are shown at negative radius, and the curves calculated from the upper righthand (UR) quadrant (for the same trial) are shown at positive radius. Both the peak value and shape of the number density profile are slightly different between the UR and LR quadrants due to the sensitivity of the inversion to the symmetry of the underlying data, though the discrepancy is insignificant against the observed trends. The values of peak density and half-width at half-maximum (HWHM) computed from each quadrant were averaged together for each trial. Due to shot-to-shot variability of the SPG device, an average of 10 trials was conducted at each operating point. The final error computed at each operating point is a combination of the two quadrants and averages across several trials.

The empirical scaling law governing the peak density as a function of the peak discharge current (I) is shown in Fig. 3(b). For a power law of the form I^α, we obtain a fit parameter of $\alpha = 1.838 \pm 0.188$. We have consistently measured

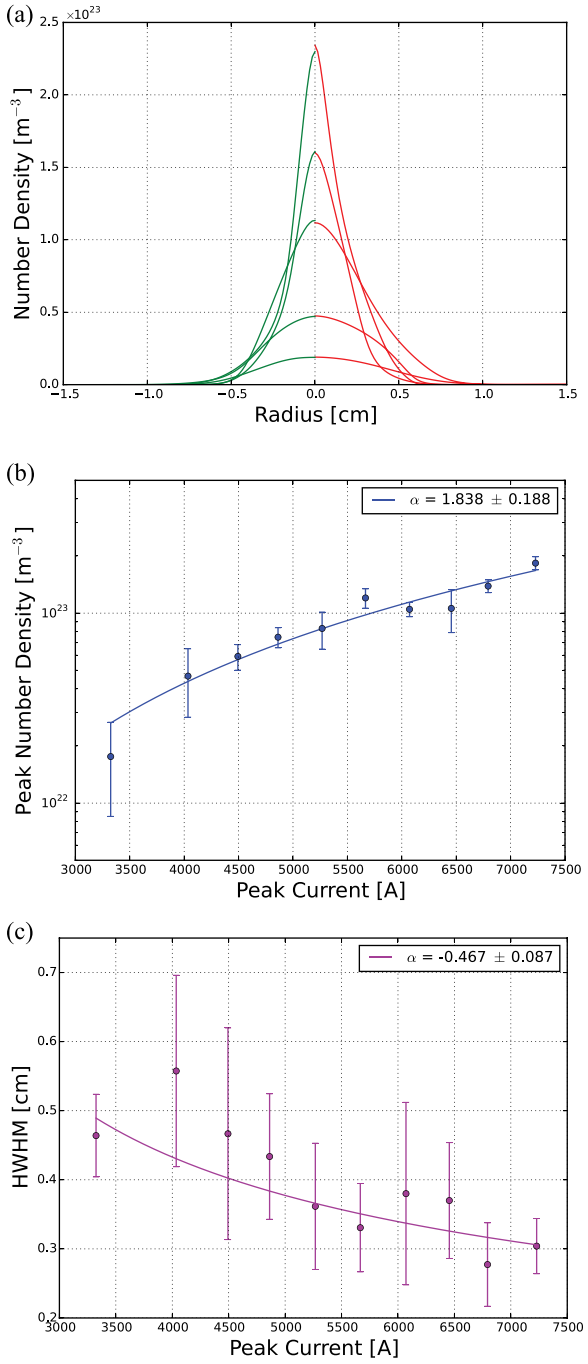

FIG. 3. (a) Selected radial density plots, based on Voigt fits of the Abel-inverted emissivity profiles, at various operating conditions. (b) Scaling of the peak number density with charging voltage, with proportionality of the form $n_e \propto I^\alpha$. (c) Scaling of the half-width at half maximum of the density profiles with charging voltage, with proportionality of the form HWHM $\propto I^\alpha$. Error bars in (b) and (c) based on average value from 10 trials at each operating point.

across all tested conditions that the measured peak discharge current is linearly proportional to the input charging voltage, which is explicitly set when operating the machine.[30] The calculated fit parameter is consistent with a scaling with magnetic pressure, which is proportional to B^2 (and thus to I^2). Results from higher current systems report densities that are 1–2 orders of magnitude higher,[29] with peak magnetic pressures that are also 1–2 orders of magnitude higher. It is likely, therefore, that the peak density scales with the radial

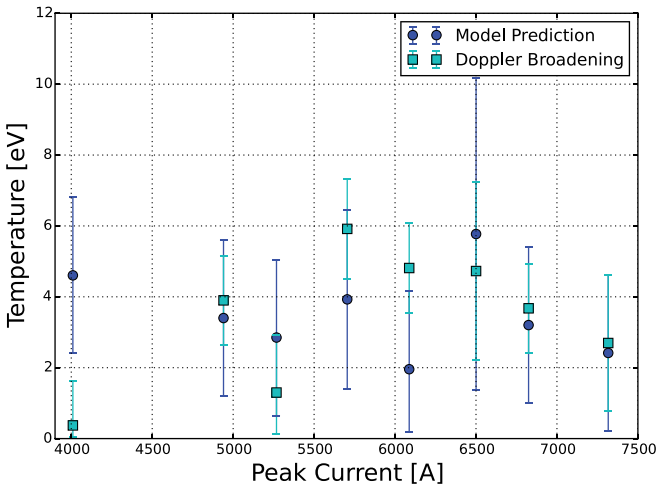

FIG. 4. Comparison of the predicted ion temperatures, based on the measured density profiles and the model described in Equations (4)–(7), with the measured temperatures based on the Doppler broadened Fe I emission line. Good agreement is obtained across the range of operating conditions, with the best agreement obtained at higher energies. Error bars based on average of 7–12 trials at each operating point.

magnetic pressure, consistent with the compressive behavior of a Z-pinch.

The scaling of the HWHM of the density profiles with peak current is shown in Fig. 3(c). The characteristic diameter of the pinch region ranges from ∼0.5–1.5 cm, inversely with the peak discharge current. In particular, the power law fit parameter is $\alpha \simeq -0.5$, or HWHM $\propto 1/\sqrt{I}$. This inverse pseudo-diffusive scaling of the density profile shape with discharge current (and magnetic field) implies an integral constraint on the density profile, indicative of the characteristic radial compression of a Z-pinch.

The strongest evidence for the formation of a radially-equilibrated Z-pinch comes from the comparison between the measured plasma temperature and the model-derived plasma temperature, the results of which are shown in Fig. 4. The measured and predicted temperatures correspond to within the estimated error (the result of shot-to-shot variability) at every operating condition except the lowest drive current. This observation can be explained by the fact that at low drive currents, the radial magnetic pressure may be too low to adequately confine the plasma, and thus the radial equilibrium model may not apply. At higher energy operating conditions, the correspondence is remarkably close. This could be the result of the increased validity of the LTE assumption at higher densities and collisionality, such that the impurity species are closer to the bulk plasma temperature, or simply that the pinch model is more applicable due to stronger compression at higher drive currents.

In summary, we have developed robust empirical scaling models for both the peak number density and the shape of the density profile in the focus region downstream of the Stanford Plasma Gun. The peak number density scales closely with the magnetic pressure, and the characteristic radius of the high density region of the pinch scales inversely with the field. Based on these observations of the jet characteristics at increasing peak drive currents, we can infer that during a single firing of the accelerator, the rising drive current pulse leads to radial plasma compression in the focal region, consistent with a Z-pinch. Using the CDV Z-pinch model, we then predict temperatures in the compression region according to the measured plasma density profiles at various operating conditions. By also deriving an estimate of the bulk plasma temperature from the Doppler broadened impurity lines, we compare the predicted and measured plasma temperatures and find them to be consistent across the majority of operating points. At operating points with higher drive currents (and thus stronger hypothetical pinching), the difference between the predicted and measured plasma temperatures diminishes. Taken in combination, both the empirical scaling laws and temperature modeling and measurement comparisons provide strong evidence of the formation of a radially-equilibrated Z-pinch within the emerging deflagration-produced jet.

This work is supported by the U.S. Department of Energy Grant No. DE-NA0002011. K. Loebner and T. Underwood gratefully acknowledge the financial support of the National Defense Science and Engineering Graduate Fellowship program. The authors would also like to thank Professor U. Shumlak and Dr. R. Golingo for their helpful discussions concerning application of the equilibrium model, as well as the members of the Stanford Plasma Physics Laboratory who have provided help and guidance to our work.

[1]J. Marshall, Phy. Fluids **3**(1), 134–135 (1960).
[2]P. F. Little and B. E. Avis, J. Nucl. Energy Part C **8**, 11 (1966).
[3]D. Y. Cheng, Nucl. Fusion **10**, 305 (1970).
[4]D. M. Woodall and L. K. Len, J. Appl. Phys. **57**, 961 (1985).
[5]J. H. Degnan, W. L. Baker, S. W. R. Warren, D. W. Price, M. P. Snell, R. J. Richter-Sand, and P. J. Turchi, J. Appl. Phys. **61**, 2763 (1987).
[6]S. Zhi-Gang, L. Cheng-Hui, L. Chun-Hian, and W. Cheng, J. Phys. D: Appl. Phys. **28**(2), 314 (1995).
[7]J. T. Bradley, J. M. Gahl, and P. D. Rockett, IEEE Trans. Plasma Sci. **27**, 1105 (1999).
[8]H. Bruzzone and J. Martínez, Plasma Sources Sci. Technol. **10**(3), 471–477 (2001).
[9]V. I. Tereshin, A. N. Bandura, O. V. Byrka, V. V. Chebotarev, I. E. Garkusha, I. Landman, V. A. Makhlaj, I. M. Neklyudov, D. G. Solyakov, and A. V. Tsarenko, Plasma Phys. Controlled Fusion **49**, A231 (2007).
[10]F. R. Poehlmann, M. A. Cappelli, and G. B. Rieker, Phys. Plasmas **17**, 123508 (2010).
[11]K. T. K. Loebner, B. C. Wang, F. R. Poehlmann, Y. Watanabe, and M. A. Cappelli, IEEE Trans. Plasma Sci. **42**, 2500 (2014).
[12]P. M. Bellan, S. You, and S. C. Hsu, Astrophys. Space Sci. **298**, 203 (2005).
[13]S. Lebedev, *High Energy Density Laboratory Astrophysics* (Springer, 2007).
[14]J. Cassibry, Y. Thio, and S. Wu, Phys. Plasmas **13**, 053101 (2006).
[15]J. T. Cassibry, R. J. Cortez, S. C. Hsu, and F. D. Witherspoon, Phys. Plasmas **16**, 112707 (2009).
[16]F. D. Witherspoon, A. Case, S. J. Messer, R. Bomgardner, M. W. Phillips, S. Brockington, and R. Elton, Rev. Sci. Instrum. **80**, 083506 (2009).
[17]U. Shumlak and C. W. Hartman, Phys. Rev. Lett. **75**, 3285 (1995).
[18]U. Shumlak, R. P. Golingo, B. A. Nelson, and D. J. Den Hartog, Phys. Rev. Lett. **87**, 205005 (2001).
[19]U. Shumlak, B. A. Nelson, R. P. Golingo, S. L. Jackson, E. A. Crawford, and D. J. Den Hartog, Phys. Plasmas **10**, 1683 (2003).
[20]D. Y. Cheng, AIAA J. **9**, 1681 (1971).
[21]K. T. K. Loebner, T. C. Underwood, A. Lucca-Fabris, M. A. Cappelli, and J. J. Szabo, in *Proceedings of the 34th International Electric Propulsion Conference* (Hyogo-Kobe, Japan, 2015).
[22]K. T. K. Loebner, T. C. Underwood, and M. A. Cappelli, Phys. Rev. Lett. **115**, 175001 (2015).
[23]R. P. Golingo, U. Shumlak, and B. A. Nelson, Phys. Plasmas **12**, 062505 (2005).
[24]K. T. K. Loebner, T. C. Underwood, and M. A. Cappelli, Rev. Sci. Instrum. **86**, 063503 (2015).

[25]O. H. Nestor and H. N. Olsen, SIAM Rev. **2**, 200 (1960).
[26]H. Ehrich and D. E. Kelleher, Phys. Rev. A **21**, 319 (1980).
[27]A. Kramida, Y. Ralchenko, and J. Reader, NIST atomic spectra database (ver. 5.0) (National Institute of Standards and Technology, Gaithersburg, MD, 2012).
[28]S. Jackson, "Density Characteristics of a Sheared-flow Z-pinch," Ph.D. thesis (University of Washington, 2006), available at http://adsabs.harvard.edu/abs/2006PhDT.....71J.
[29]U. Shumlak, R. P. Golingo, M. C. Hughes, S. D. Knecht, W. Lowrie, N. Murakami, B. A. Nelson, M. C. Paliwoda, and M. P. Ross, in *Proceedings of the 2012 Abstracts IEEE International Conference on Plasma Science* (IEEE, 2012), p. 2P–94.
[30]See supplementary material at http://dx.doi.org/10.1063/1.4943370 for detailed results of imaging spectrometer calibration and I-V proportionality.